Predicting ocean-induced ice-shelf melt rates using a machine learning image segmentation approach

Sebastian H. R. Rosier[1,2], Christopher Y. S. Bull[1], and G. Hilmar Gudmundsson[1]

[1]Department of Geography and Environmental Sciences, Northumbria University, Newcastle Upon Tyne, UK
[2]WSL Institute for Snow and Avalanche Research SLF, Davos, Switzerland

Correspondence: Sebastian Rosier (sebastian.rosier@northumbria.ac.uk)

Abstract. Through their role in buttressing upstream ice flow, Antarctic ice shelves play an important part in regulating future sea level change. Reduction in ice-shelf buttressing caused by increased ocean-induced melt along their undersides is now understood to be one of the key drivers of ice loss from the Antarctic Ice Sheet. However, despite the importance of this forcing mechanism most ice-sheet simulations currently rely on simple melt-parametrisations of this ocean-driven process, since a fully

5 coupled ice-ocean modelling framework is prohibitively computationally expensive. Here, we provide an alternative approach that is able to capture the greatly improved physical description of this process provided by large-scale ocean-circulation models over currently employed melt-parameterisations, but with trivial computational expense. We introduce a new approach that brings together deep learning and physical modelling to develop a deep neural network framework, MELTNET, that can emulate ocean model predictions of sub-ice shelf melt rates. We train MELTNET on synthetic geometries, using the

10 NEMO ocean model as a ground-truth in lieu of observations to provide melt rates both for training and to evaluate the performance of the trained network. We show that MELTNET can accurately predict melt rates for a wide range of complex synthetic geometries and outperforms more traditional parameterisations for >95% of geometries tested. Furthermore, we find MELTNET's melt rate estimates show sensitivity to established physical relationships such as a changes in thermal forcing and ice shelf slope. This study demonstrates the potential for a deep learning framework to calculate melt rates with almost

15 no computational expense, that could in the future be used in conjunction with an ice sheet model to provide predictions for large-scale ice sheet models.

1 Introduction

Ocean induced melting of ice shelves is currently the main driver of ice mass balance change in Antarctica and represents a major source of uncertainty for predictions of future sea level rise (Pritchard et al., 2012; Shepherd et al., 2018; Edwards

20 et al., 2021; IPCC, 2021). Enhanced melting, resulting in a decrease in ice shelf thickness, can lead to a reduction in the buttressing force that ice shelves impose on the ice sheet and thereby a net increase in mass loss (Thomas, 1979; Dupont and Alley, 2005; Gudmundsson et al., 2012). Strong feedbacks between melt rates, the cavity geometry, and ocean circulation can lead to complex temporal and spatial heterogeneity at many different scales, so modelling these processes is challenging (Donat-Magnin et al., 2017; De Rydt et al., 2014; Jordan et al., 2018; Smith et al., 2021; Kreuzer et al., 2021). The current

25 generation of ice sheet models employ different approaches to deal with this problem and these can broadly be split into three
main categories: (1) simple parameterisations that depend on one or more local quantities (e.g. ice shelf draft), (2) intermediate
complexity parameterisations that incorporate local and nonlocal processes and include some basic physics of the circulation in
an ice shelf cavity (some examples are described later) and (3) ocean general circulation models that are able to capture most of
the processes leading to melting at the ice shelf base (Favier et al., 2019). Each of these approaches comes with advantages and

30 disadvantages but broadly speaking the main tradeoff is computational expense vs. fidelity to our best current understanding of
ocean circulation within an ice-shelf cavity.

Difficulties in capturing complex physical processes within large scale models is not a problem unique to glaciology. A large
source of uncertainty in global climate models running at standard resolution arises from an inability to resolve important cloud
processes or accurately calculate convection (Stevens and Bony, 2013). Higher resolution models that do, running at up to 1km

35 resolution, are too expensive to run for longer than one year (Khairoutdinov and Randall, 2003, e.g.). A very recent innovation
in these fields is to train a neural network, using high resolution models, to parameterise these processes more accurately in
a coarser resolution model (Rasp et al., 2018; O'Gorman and Dwyer, 2018; Brenowitz and Bretherton, 2018, 2019, e.g.). In
this way, the fidelity of physical models running at lower resolution, tractable for long term global prediction, can be greatly
improved with almost no additional computational cost.

40 In a similar vein, a major hurdle for modelling efforts of the Antarctic Ice Sheet is the considerable difference in timescales at
which changes occur in the ice sheet and the surrounding ocean. To provide accurate prediction and retain numerical stability,
large-scale ocean models typically require timesteps of $\mathcal{O}(10^2 - 10^3 s)$ whereas ice sheet models can often be run at timesteps
of $\mathcal{O}(10^7 s)$ or more. This disparity means that simulations that couple an ocean model to an ice sheet model are severely
constrained in simulation time and are typically restricted to making predictions for hundreds of years (e.g. Jordan et al., 2018;

45 Thoma et al., 2015; Seroussi et al., 2017; Naughten et al., 2021). That restriction is pertinent, since the full extent of committed
sea level rise arising from a changing climate takes millennia to manifest itself in ice sheet models (Garbe et al., 2020). In
addition, the computational cost of the ocean models is restrictive and coupled ice-ocean models are often limited to regional
simulations, precluding the ability to model how retreat of one basin affects a neighbouring basin. A third and perhaps most
important drawback of this high computational cost is that coupled studies typically rely on a smaller set of simulations which

50 cannot properly sample the model parameter space, making it very hard to calculate uncertainty estimates which are now
widely recognised as a vital component of predictions.

Despite the numerous drawbacks in using a coupled approach, ocean models present a significant advantage in their ability to
reproduce the complex physical processes that lead to melt rate patterns beneath an ice shelf. Capturing the spatial distribution
accurately is important because relatively small regions of an ice shelf are disproportionately important to the transient response

55 of ice flow (Goldberg et al., 2019). Simpler parameterisations can be tuned to better match observations to some extent but
it is not clear that these tuned models remain valid for longer simulations as the ice sheet geometry and ocean conditions
diverge significantly from their present day configuration. Were a paramterisation to exist that did not require tuning, this
would represent a major step forward in long-term predictions for the future of the Antarctic ice sheet.

Given the current gulf between ocean models and lower complexity parameterisations, and the aforementioned problems with making long-term forecasts for the Antarctic ice sheet using a fully-coupled approach, there is a clear need for an alternative middle ground. This should retain the ability to predict complex spatial patterns of melting but be computationally efficient in order to be able to run it synchronously with an ice sheet model without inhibiting the size of the domain or the duration of the simulation. Here, we propose using deep learning to emulate ocean model behaviour for the prediction of sub ice-shelf melt rates. Since the computational cost of a machine learning algorithm is insignificant once it has been trained, this could provide an alternative modelling approach. By treating the ocean model as a ground-truth and running ocean simulations on a wide variety of ice shelf configurations and ocean conditions, a network can be trained to approximate the behaviour of an ocean model. As a first step towards this goal, we demonstrate a deep learning framework that can accurately reproduce melt rate patterns as predicted by the NEMO ocean model and shows significantly better performance than existing intermediate complexity parameterisations without any increase in computational cost.

2 Models and Methods

In the absence of sufficiently large observational melt rate training data sets for effective deep learning, we generate entirely random and synthetic geometries, together with temperature and salinity forcing, for several thousand ice shelves. These inputs are used as forcings for NEMO, a general circulation ocean model, which gives a simulated ice shelf melt rate. The inputs and NEMO melt rates are then applied within our deep learning framework, MELTNET, to train a model that can predict melt rates that closely resemble those predicted by the NEMO ocean model. We hold back 5% of the generated inputs, which are not shown to the network during training and so can be used both to evaluate MELTNET and compare its performance with other melt rate parameterisations. We begin by describing our deep learning methodology, followed by the NEMO ocean model. We then explain how the synthetic input fields, consisting of ice shelf geometry, bathymetry, temperature and salinity fields, are generated. Finally, we introduce the two intermediate complexity melt rate paramterisations that we compare MELTNET performance against.

2.1 Deep learning methodology

Our deep learning approach consists of two separate neural networks, trained to perform the two steps required to go from input fields to a melt rate field. All network design and training was done using MATLAB's deep learning toolbox (The MathWorks, 2021). In the first step, input geometries and ocean conditions (Sec. 2.3), together with NEMO melt rates (Sec. 2.2), are used to train a segmentation network that learns to classify regions of an ice shelf with labels representing the magnitude of melting or refreezing. Secondly, an autoencoder network is trained to convert from these discrete classified melt rates to a continuous melt rate field. Hereafter, we refer to the combination of these two networks working in tandem, which together form our proposed melt rate parameterisation, as MELTNET. Figure 1 shows the workflow for training each network and predicting melt rates and each of these steps is described in more detail below.
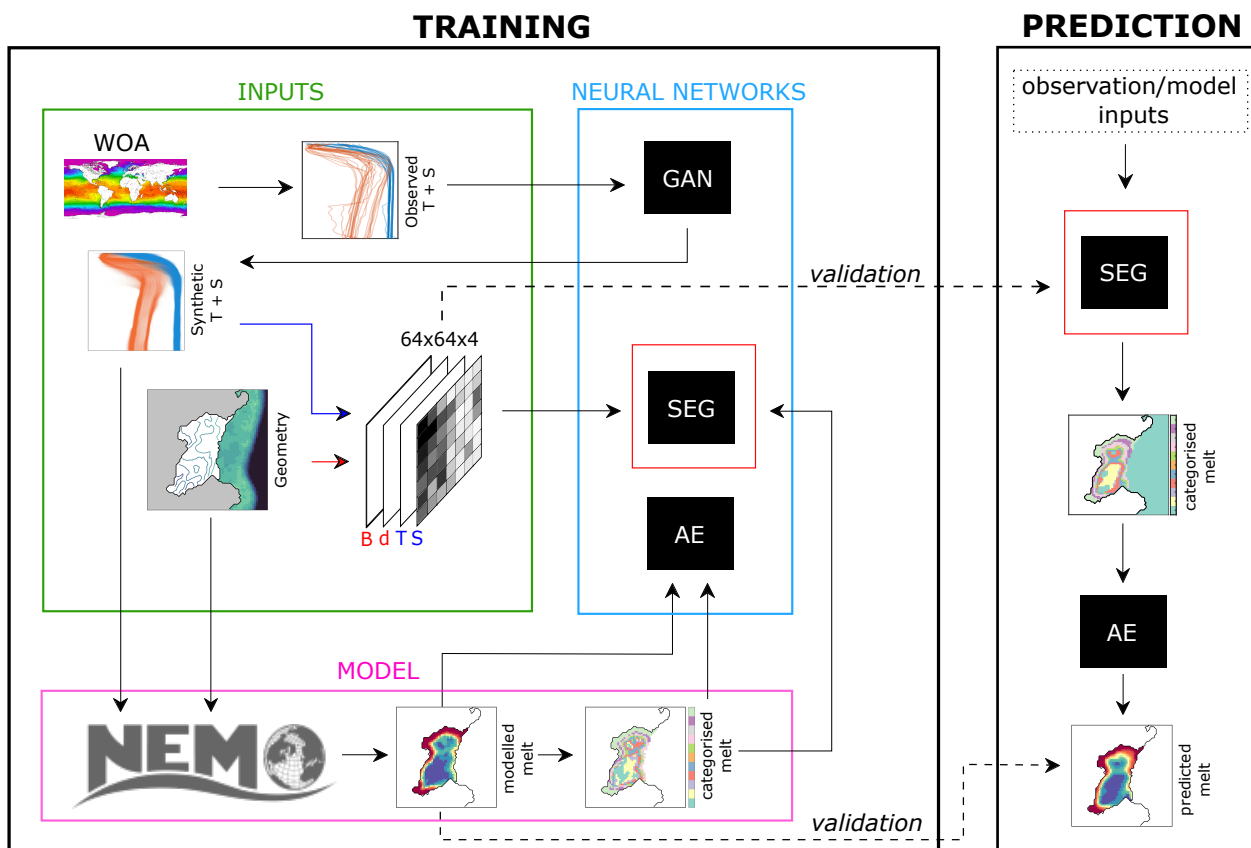
Figure 1. Workflow diagram for the proposed deep learning framework, split into training and prediction. Synthetic ice shelf geometries (Section 2.3.1) and synthetic temperature and salinity profiles generated from WOA data (Section 2.3.2) are used (1) as inputs for the NEMO model which predicts a melt rate field and (2) to create a four channel input image for training of the segmentation network. NEMO melt rates are converted into a labelled image and the segmentation network trains to segment input images that match labelled NEMO output. Separately, the autoencoder network takes the melt rate map and labelled melt rates from NEMO and learns to map between the two. In both of these networks, 5% of inputs and NEMO melt rates are withheld to form the validation set. Once the networks are trained, melt rate prediction proceeds by passing input images to the segmentation net and the resulting labelled images to the autoencoder, leading to a melt rate field.

2.1.1 Segmentation

The primary network, designed to classify melt rates from an input image, is a modified version of the SegNet architecture proposed by Badrinarayanan et al. (2017), with the modified architecture shown in Fig. B1. A segmentation network takes images as input and assigns a label to each pixel of that image. That input image may have different numbers of bands, for

example a black and white image would have one input band and a standard colour image would have three. In our case, we use
95 input images with 64x64 pixels and four bands representing bathymetry, ice shelf draft, temperature and salinity. Note that the
methodology is completely flexible with regards to the size of the image and the number of bands so more information could be
coded into additional bands, as discussed later. In MELTNET, each pixel may have a value from 0 to 255 and geometrical input
fields are re-scaled and mapped directly into the first two bands. Mapping of the temperature and salinity forcing, which are
defined as depth dependant but spatially independent boundary conditions for the ocean model, is less intuitive. We explored
100 several different options, all of which involved taking the depth-varying temperature and salinity and mapping those directly
to the ice shelf base at equivalent depth. Two noteworthy options we tested are: using the temperature and salinity profiles that
NEMO is forced (prescribed) with at the boundary, or using the temperature and salinity simulated by NEMO at the ice front.
In practice, we found that it made little difference to the segmentation network accuracy (92.6% classification accuracy vs.
93.4%, respectively). We decided then, that taking average temperature and salinity conditions at the ice shelf front after model
105 spinup was most consistent with existing melt rate parameterisations, since this is akin to forcing our model with observations
near the relevant ice shelf. These mapped temperature and salinities are then re-scaled and form the remaining bands of our
input image.

The target melt rate field output by NEMO (Sect. 2.2) must be converted to a labelled image with a finite number of classes in
order to be used to train the segmentation network. A tradeoff exists when selecting the number of classes for the segmentation
110 network and the final performance of MELTNET in terms of predicting melt rates. With fewer classes, the segmentation net
accuracy goes up but the inverse classification net struggles to infer complex melt rate patterns, whereas with more classes
the segmentation net accuracy drops, also resulting in a drop in overall MELTNET performance. We tested networks using
$N = 5$ to 11 classes and the resulting NRMSE (Normalised Root Mean Squared Error, described later) varied from 0.16 to
0.12. Based on this testing, an optimal number of classes for our training set was found to be $N = 8$. Melting (or freezing)
115 rates were converted to N discrete melt labels by calculating $N - 2$ quantiles of melt rates for every pixel in the training set
and assigning labels to melt rates that fall between each quantile, with the last label reserved for regions of the image with no
melt/refreezing (i.e. outside of the ice shelf).

The segmentation net takes these input images and the corresponding set of labelled melt rates from NEMO and learns to
reproduce the labelled melt rate distribution. At its core are convolutions, consisting of sets of filters that operate on the image.
120 These filters are learned during the training, using stochastic gradient descent to minimise the loss function which is calculated
by comparing the output with the NEMO training set. Layers of filters learn to extract useful features at different scales within
the image, for example the outline of the coast or the local slope of the ice shelf base. The final training set, once a small
subset of anomolous NEMO simulations with extreme temperatures were removed, consisted of 2575 images, with a further
136 ($\sim$5%) retained for validation. MELTNET accuracy increases with an increasingly large number of training images but by
125 testing incrementally larger training sets this number was found to be sufficient (Fig. B4).

The majority of each input image consists of pixels that lie outside of the ice shelf extent, resulting in a large bias in the
training and scoring of the network towards pixels that are of no interest to our application. To alleviate this issue, classes were
weighted according to the total frequency of pixels in each class for the entire training set. Furthermore, a random rotation

of either 0°, 90°, 180° and 270° was applied to each input image, to ensure that the network learns to predict melt rates
130   independently of geometrical orientation. Occasionally, when training for larger numbers of epochs, the segmentation network
would stop labelling certain categories. This was determined to result from vanishing gradients in certain neurons and to
alleviate this issue, all ReLU (Rectified Linear Unit) activation function layers in the network were replaced with swish layers,
which have the form $f(x) = x \cdot \mathrm{sigmoid}(x)$, as these have been found to consistently outperform the more common ReLU
function (Ramachandran et al., 2017).

2.1.2   Inverse classification

We use another deep learning approach to perform the task of converting from discrete melt labels, output by the SegNet, to a
continuous melt rate field. We found that a modified denoising autoencoder (DAE) architecture, based on the network proposed
by Zhang et al. (2017), was able to perform this task effectively. DAEs take partially corrupted input and are trained to extract
features that capture useful structure in order to recover the uncorrupted original. In this case, the corruption is the process of
140   categorising melt rates into N discrete labels, which results in images that retain much of the original melt rate pattern but lose
fine-scale detail and magnitude information. The segmentation net is trained on these labelled melt rate images rather than the
NEMO output directly, and itself outputs the same labels which need to be converted back to a continuous melt rate field in
order to provide useful output for an ice sheet model.

The training set consists of labelled NEMO melt rates as inputs and true NEMO rates as outputs, i.e., the DAE learns to map
145   from discrete labels to a continuous melt rate field. The specific experiments that comprised training and validation sets were
the same as those used to train the segmentation network. This ensured that the DAE did not get any unfair advantage from
having already seen similar melt rate patterns during its training as those output by the segmentation net. The DAE architecture
consists of several layers of 2D convolutions, batch normalisations and Swish layers (Swish layers were found to considerably
improve performance compared to ReLU layers), as shown in Fig. B2. A comparison between NEMO melt rates, those same
150   NEMO melt rates converted to a labelled image and the result of mapping from labelled images to melt rates using the trained
DAE network is shown in Fig. B3.

2.2   NEMO Ocean modelling

The ocean general circulation model used in this study is version v4.0.4 of the Nucleus for European Modelling of Ocean
model (NEMO; Madec and Team). NEMO solves the incompressible, Boussinesq, hydrostatic primitive equations with a split-
155   explicit free-surface formulation. NEMO here uses a z*-coordinate (varying cell thickness) C-grid with partial cells at the
bottom-most and top-most ocean layers in order to provide more realistic representation of bathymetry (Bernard et al., 2006)
and the ice-shelf geometry, respectively. Our model settings include: a 55-term polynomial approximation of the reference
Thermodynamic Equation Of Seawater (TEOS-10; IOC and IAPSO (2010)), nonlinear bottom friction, a free-slip condition at
the lateral boundaries (at both land and ice shelf interfaces), energy- and enstrophy-conserving momentum advection scheme
160   and a prognostic turbulent kinetic energy scheme for vertical mixing. Laterally, we have spatially varying eddy coefficients
(according to local mesh size) with a Laplacian operator for iso-neutral diffusion of tracers and a biharmonic operator for

lateral diffusion of momentum. Our model setup utilises the ice-shelf module that was developed by Mathiot et al. (2017). Calculation of the ice shelf melt rate follows the standard three-equation parameterization as described in Asay-Davis et al. (2016), with heat exchange and salt exchange coefficients of $\Gamma_T = 6 \times 10^{-2}$ and $\Gamma_s = 1.7 \times 10^{-3}$, respectively. Additionally,

165 the top drag coefficient is $C_d = 2.5 \times 10^{-3}$. The conservative temperature, absolute salinity, and velocity are averaged over the top mixed layer, defined here as a 20-m layer at the top of the cavity (or the entire top level where top levels are thicker than 20 m). The ice shelf thickness is static, so it is assumed that the ice dynamics instantaneously compensate melt-induced thinning.

The modeling domain is on a beta-plane with 64 regularly spaced points in both x and y, spanning ∼502 km (horizontal resolution of ∼8 km). The ocean floor is limited to 2000m and is represented by 45 vertical levels. Walls exist on all four

170 boundaries where the only external forcing is a restoring condition at the northern boundary, where the restoring is towards the initial state. The simulations are initialised from rest with initial conditions taken from the synthetic temperature and salinity fields described in Sect. 2.3.2, these fields then also set the northern restoring condition as simulation evolves. The configuration has no: surface forcing, sea ice and tides, but is inspired by the idealised ISOMIP+ experiments of Asay-Davis et al. (2016), where the interest here was to have a simple system in which to test the capabilities of a neural network to predict melt rates

175 within drastically idealised ice shelf cavities. Future work will look at extending the neural network to more complex systems. Following Holland et al. (2008), all simulations in this paper have a common spin-up of ten years where the time-mean values of the final year are used for all analysis. Sensitivity tests (not shown) suggest that a 10 year spin up is sufficient to capture the equilibrated response of the ice shelf to the forcing.

2.3 Synthetic input generation

180 A major hurdle to overcome with this deep learning approach is to generate synthetic inputs that are realistic but also show sufficient variability to be useful analogs to real ice shelves. This problem can be broken down into two main steps; generation of the ice shelf geometry and generation of the temperature and salinity fields which set both the ocean initial conditions and far field restoring.

2.3.1 Ice shelf and coastline geometry

185 Four steps are involved in creating the geometry of the bathymetry (including the coastline) and ice-shelf draft, the algorithm consists of:

1. Create an outline of the coast;

2. Define the ice-shelf and continental shelf horizontal extent;

3. Define ice thickness at the grounding line and then generate ice shelf draft;

190 4. Define bathymetry, constrained by features generated in preceding steps.
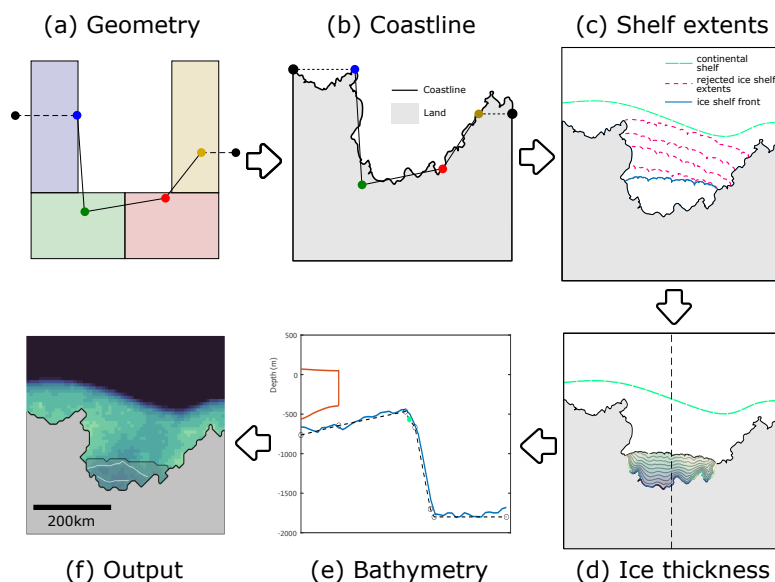
Figure 2. Flowchart showing the steps leading to generation of a random ice shelf geometry, consisting of (a) generation of corner nodes randomly located within the four coloured polygons, (b) creation of a continuous fractal coastline, (c) definition of ice shelf and continental shelf horizontal extents, (d) definition of ice thickness at the grounding line and from this the full 2D ice shelf draft, (e) generation of a bathymetry constrained by the previous steps, leading to (f) one randomly sampled ice shelf geometry (background colourmap represents ocean bathymetry and contours are ice shelf draft, following the same ranges as in Fig. 3).

Each of these steps generates one or more random numbers that determine some geometrical property of the final domain, leading to a very large variety of final ice shelf configurations. These steps will now be outlined in order, with each step in its own paragraph.

   The starting point for generating ice shelf geometries is the observation that most Antarctic ice shelves, particularly large
195 ones, occur within embayments along the coast, while some smaller unconfined ice shelves also exist along flatter sections of the coastline. From a square domain, we start by creating a polygon that will define the overall geometry of the coastline from four random point seeds that can each lie anywhere within their four predefined boxes, as shown in Fig 2a. Two further points are added on either side and inline with the previous end points to create a polygon with six points and five edges. Due to the extents of the four boxes within which the four initial points are seeded, most geometries will consist of a central embayment
200 but the concavity of the resulting bay can vary from almost flat to a deep and strongly confined. This simple polygon is then transformed into a complex polygon more closely resembling the fractal nature of a real coastline by repeatedly adding points midway between two existing points and offset some random distance from that edge, resulting in a final coastline as shown in Fig 2b.

   With a coastline defined as described above, the next step is to define plausible extent for the ice-shelf front and from this the
205 continental shelf break. Points on the coastline nearest to the two corner points (blue and yellow points in Fig 2a) are selected

as trial start and end points for the ice-shelf front which has a random curvature (this determines the ice-shelf front shape, from concave to convex). If the ice-shelf front polygon does not intersect any coastline points and the area is less than a randomly selected minimum area then the ice-shelf front is accepted. If the ice shelf front is rejected, the two starting points along the coast for the calving front polygon are moved closer together and the procedure is repeated until a geometry is accepted. This

210 results in a variety of different sized ice shelves that tend to be confined by any existing embayment in the coast. As a next step, a distance is calculated for each open ocean point and the combined ice front and coastline ocean boundary. A contour of constant distance from the coastline is then drawn and converted to a tensioned spline to generate a smooth polygon that defines the continental shelf break. The result of these two steps is shown in Fig 2c.

The geometry is now fully defined in 2D, but requires information on ice and water column thickness to be used as input for

215 the ocean model. Ice thickness is first defined everywhere along the ice shelf grounding line as a product between distance to the ice front, a measure of the coastline curvature and a random factor (resulting in a maximum ice thickness at the grounding line of 2000 m). This leads to ice thicknesses that are generally greater further from the coast and particularly where the coast consists of smaller inlets, to mimic plausible ice streams flowing into the ice shelf. Ice thickness is then extrapolated at regular points along the grounding line to the ice front using a simple analytical expression for a buttressed ice shelf thickness profile

220 from Nilsson et al. (2017) under the simplifying assumption of no net accumulation. These ice thickness profiles are combined and mapped onto a grid to generate a 2D ice thickness field everywhere within the ice shelf (Fig 2d).

The ice thickness and continental shelf are used to constrain the ocean bathymetry by constructing polygons at regular intervals through the domain. Points at 2000 m depth are added at the open ocean boundary and a fixed distance from the shelf break. Further points are added around the shelf break at depths controlled by the ice shelf draft at the ice front and a final point

225 is added at the grounding line at 200 m below the grounding line depth. The polygons are combined to form a grid of depths and random brownian noise is added to generate the final bathymetric grid (Fig 2e). The resulting fields of ice thickness and ocean depth are generated at finer resolution and then linearly interpolated onto 64x64 grids which serve directly as inputs to the ocean model (with each cell representing ∼8x8 km) and their discretised form serve as two bands of the input images for the segmentation net (Fig 2f).

230 A sample of 36 synthetic domain geometries is shown in (Fig 3). The algorithm that generates synthetic ice shelf geometries must be capable of creating a wide variety of configurations. Validating these geometries is not possible, however the resulting configurations are visually similar to ice shelves typically found around Antarctica and the generation of ice thicknesses for each geometry, which melt rates are highly sensitive to, is based on analytical solutions for ice shelf flow. The final 64x64 grids result in each domain having an area of ∼252,000km. Given that much of the domain is taken up by grounded ice/ocean, this

235 results in maximum ice shelf areas which are less than the two largest ice shelves in Antarctica (the Ross and Filchner-Ronne Ice Shelves) but comparable to the next largest, such as the Amery and Larsen Ice Shelves.

2.3.2   Temperature and salinity forcing

The ocean model configuration used here (Section 2.2) requires a temperature/salinity restoring condition designed to imitate the far-field ocean forcing of an ice shelf. In this case, the restoring condition is applied only at the northern boundary, similar
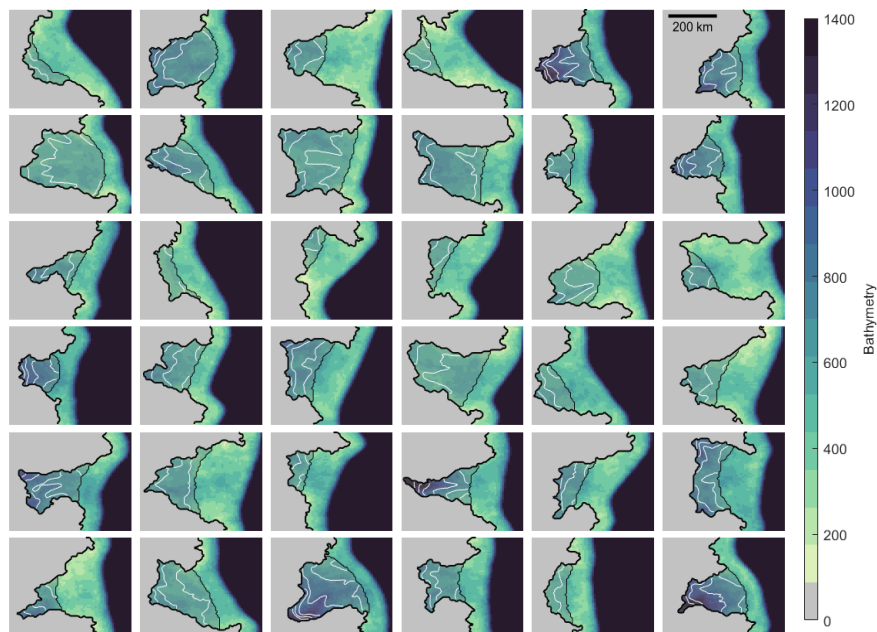
Figure 3. Sample of synthetic geometries produced using the algorithm outlined in Section 2.3.1. Grey delineates grounded ice and the colourmap represents seafloor bathymetry. White lines show ice shelf draft, contoured from 200 to 800 m at 100 intervals, and black lines show the outline of the ice sheet and ice shelf regions.

to the ISOMIP+ experiments (Asay-Davis et al., 2016). We thus need temperature and salinity fields that represent the variety of conditions that might be found in this location around Antarctica. To this end, we use the World Ocean Atlas 2018 (hereafter WOA; Boyer et al.) to extract temperature and salinity profiles around all of Antarctica. For each meridian in the gridded data, we take data from the first ocean grid cell north of the Antarctic coast that has a depth of more than 2000 m. While this results in several hundred vertical profiles that could be used directly to force our synthetic geometries, the WOA dataset is still inherently a finite source of temperature and salinity data. As an alternative, we use these data as a starting point to generate synthetic temperature and salinity profiles that share the same characteristics but can be unlimited in number and variety. This is accomplished with a Generative Adversarial Network (GAN, Goodfellow et al. (2014)). Details on this GAN network, together with a comparison between observed and generated temperature and salinity profiles, can be found in Appendix A.

2.4 Alternative melt rate parameterisations: PICO and PLUME

The performance of MELTNET is compared to two intermediate complexity melt rate parameterisations, where all models judged on their ability to match NEMO's melt rate fields. The parameterisations are the Potsdam Ice-shelf Cavity mOdel (PICO, Reese et al. (2018a)) and a 2D implementation of the plume model (Jenkins, 1991) based on Lazeroms et al. (2018) (referred to hereafter as PLUME). The PICO model includes a representation of the vertical overturning circulation within

an ice shelf cavity with a series of boxes that transfer heat and salt from the grounding line to the ice front. The PLUME

255   model adapts 1-D plume theory by selecting a melt plume origin at any given ice shelf point and determining melt rate as a

function of properties at this plume origin and local ice shelf conditions. Plume origin for every ice shelf point is selected as

the closest grounding line point, scaled by grounding line depth so that deeper origin points are favoured. Many other melt

rate parameterisations exist but these were selected since they are generally regarded as the more advanced parameterisations;

including physics related to cavity circulation while still remaining computationally inexpensive (Favier et al., 2019; Jourdain

260   et al., 2020). For both paramterisations, a high resolution version of the synthetic geometries was converted to a finite element

mesh and the Ua ice-flow model implementation of each model was used to calculate melt rates.

In order to make our comparison to the PLUME and PICO models as fair as possible, two uncertain parameters in each model

were optimised using the full set of NEMO outputs. For the PICO model, these two parameters were the overturning strength

(C) and the heat exchange coefficient (γ_T^*), which are also treated as tunetable parameters in the original PICO paper (Reese

265   et al., 2018a). For the PLUME model, the heat exchange parameter Γ_{TS} (similar but not the same as the γ_T^* parameter for

PICO) was selected, together with the plume entrainment coefficient (E_0). The PLUME and PICO models were run using the

input geometry, temperature and salinity fields and then a total Normalised Root Mean Squared Error (NRMSE) was calculated

compared to NEMO melt rates. This procedure was repeated, updating the model parameters to minimise total NRMSE, to

derive an optimal set of parameters for each model that most closely replicated the NEMO melt rates. The optimised values of

270   all intermediate complexity model parameters, together with the values originally suggested in their corresponding papers, are

shown in Table B1.

3   Results

Figure 4 presents our main result of the study, a grid of different geometries (row 1) and corresponding melt rates (m yr^{-1}) as

calculated by: NEMO (row 2), MELTNET (row 3), PICO (row 4) and PLUME (row 5). Melt rates calculated by MELTNET

275   clearly stand out amongst the lower three panels as the best qualitative match to the NEMO ocean model. In order to represent

the range of performance, rather than just the best results for any particular parameterisation, we assign a score to each MELT-

NET result and sample evenly from the distribution of results by calculating the quantiles of the scores. The score used here

(row 6), is based on a combination of the NRMSE and correlation coefficient; the two quantities are treated as vectors whose

length is scaled such that a vector of zero length is a perfect score (NRMSE of 0 or correlation coefficient of 1) and the score is

280   the L2 norm of these two vectors. Row 6 of Fig. 4 therefore shows the scores for all validation experiments ($N = 136$) in blue

and the specific experiments sampled from the distribution of these scores, that are shown in remaining panels, are marked

in red. Panels for individual experiments are sorted by increasing score from left to right. In the bottom left corner of each

panel we show the averaged melt rate as calculated by each model. Only geometries from the validation set, i.e. geometries

that MELTNET did not see during training, are included in this comparison.

285   Model performance as measured by NRMSE and correlation coefficient is shown for the three models and for all members

of the validation set in Fig. 5. Model misfit, in terms of NRMSE, was lowest with MELTNET for 95% of the members of the
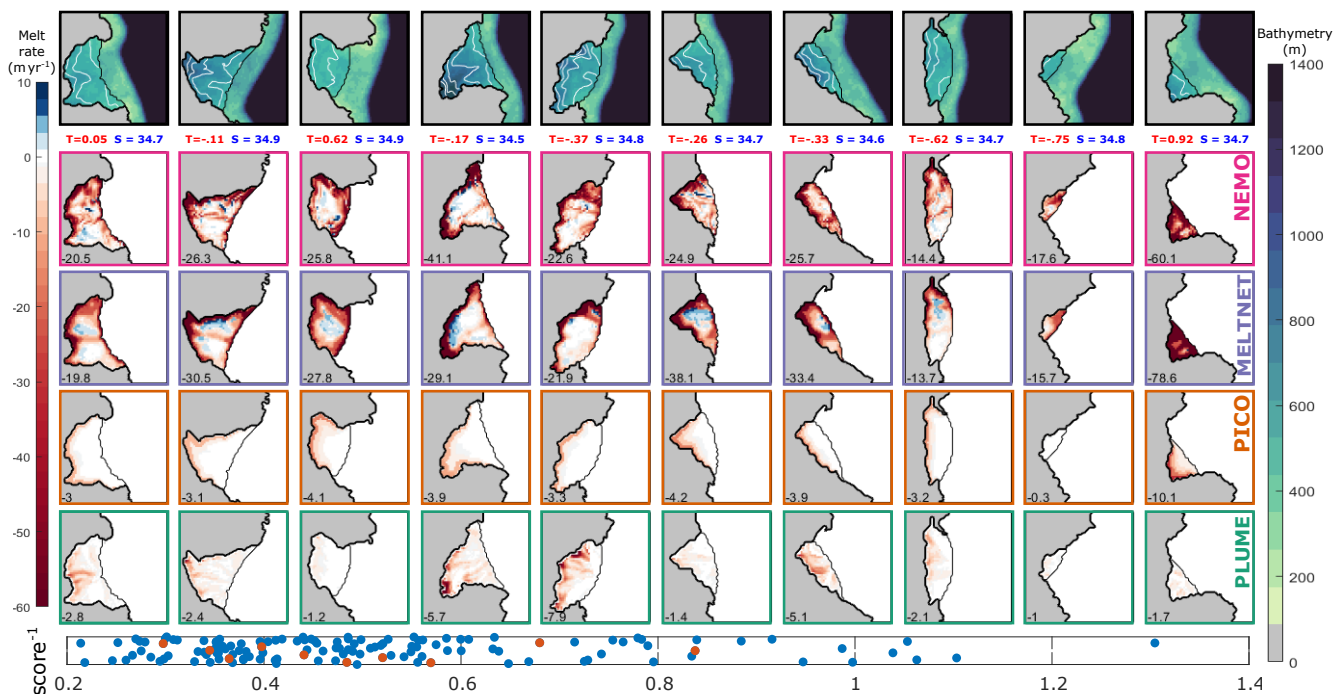
Figure 4. Input geometry (row 1) for a sample of synthetic ice shelves and the resulting melt rates (m yr^{-1}) as calculated by NEMO (row 2), MELTNET (row 3), PICO (row 4) and PLUME (row 5). Experiments were selected by sampling evenly from the distribution of MELTNET scores (all scores are shown in blue in row 6 and the sampled experiments are highlighted in red). Background colourmap for the geometries shows ocean bathymetry (scale on the right hand side) and white lines show ice shelf draft, contoured from 200 to 800 m at 100 intervals. Melt rate results all use the same colourmap, with red and blue indicating melting and refreezing, respectively. Note the colour map gradient is not linear, but is greatest around zero, to make it easier to distinguish the magnitude of melting/refreezing over the bulk of the ice shelves. Numbers in red and blue at the top of each melt rate column show the area averaged sub-ice-shelf temperature and salinity, respectively. Numbers in the bottom left corner of each melt rate panel show the averaged melt rate as calculated by each model. Both the PICO and PLUME models show results using optimised parameters (Table B1).

validation set (panel a). Pearson correlation coefficient between MELTNET and the NEMO model (mean 0.65) was higher than PICO (mean 0.14) and PLUME (0.10) for 99% of the members of the validation set (panel b). These results show that MELTNET not only has a lower misfit than the other models but is far better at reproducing spatial patterns i.e. getting melting

290 and refreezing in the right areas of each ice shelf.

A commonly raised and sensible concern with all forms of deep learning is that poorly trained networks can give the right answer for the wrong reasons. We take a number of steps to avoid this issue, for example, we randomly rotate the ice shelf orientation so that the network does not learn to associate high melting with grid cells on one side of the domain. We can also explore how MELTNET's predictions compare to our understanding of the physics underlying ocean-ice shelf interactions.
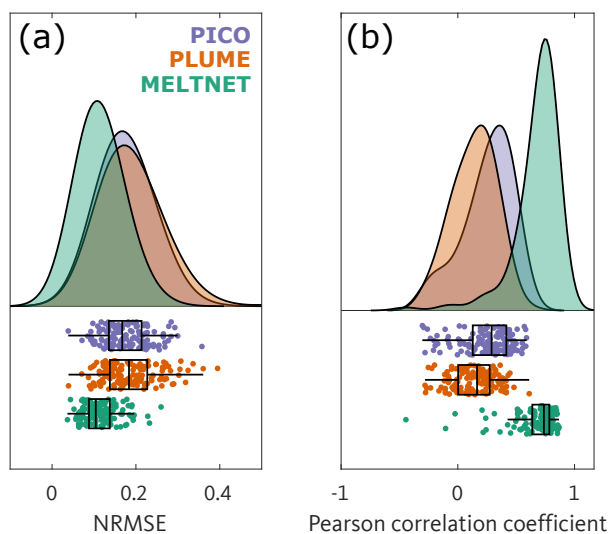
Figure 5. Distributions of NRMSE (panel a) and Pearson correlation coefficient (panel b) for the three different melt rate parameterisations: PICO (violet), PLUME (orange) and MELTNET (green). The lower section of each panel shows each individual score from the entire validation set, overlain with a boxplot. The box represents the interquartile range of scores and the vertical line through the box is the median. The upper section of each panel presents the same information as probability density plots. Note lower NRMSE and higher correlation coefficient mean a better fit to the groundtruth NEMO melt rates.

295   This is done for a simplified ice shelf geometry, i.e., uniform bathymetry at a depth of 1100m and an ice shelf 160km long and 352km wide. Ice shelf draft varies linearly from 600m at the grounding line to 200m at the ice front and there is no across-shelf variation in the geometry. Furthermore, both salinity and temperature are constant throughout the entire domain, and as before, this forms the northern boundary restoring condition. In this context, two simple relationships are expected to emerge: (1) a linear dependency of melt rates to changes in ice-shelf slope (Jenkins, 2018) and (2) a quadratic dependency of melt rates

300   to changes in ocean temperature (Holland et al., 2008). To investigate these two relationships, we: (1) vary ice shelf basal slope by keeping grounding line depth constant and moving the ice front and (2) vary temperature by a uniform amount in the entire domain. The change in the ice-shelf cavity melt rate for these two sensitivity tests is shown in Fig 6. In both tests, the dependence matched that expected by theory, as shown by the linear and quadratic trend lines through the sample points. This goes some way to demonstrating that MELTNET has learnt an accurate representation of actual melt physics. This is in spite of

305   the fact that these simplified domains are very different from the more complex geometries that the network has been trained on.
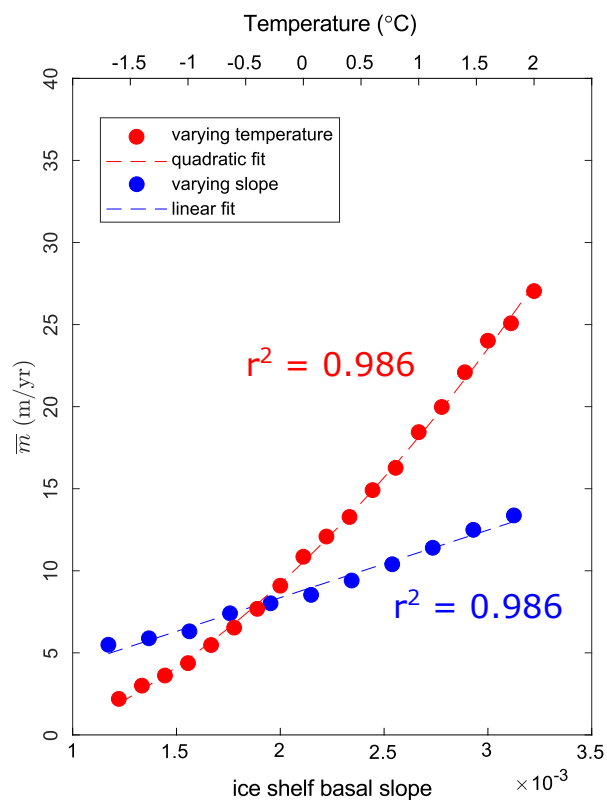
Figure 6. Area averaged basal melt rate from MELTNET for an idealised ice shelf geometry as a function of changes in ocean temperature (red) and ice shelf basal slope (blue). Dashed lines show quadratic and linear fits to results, with corresponding r^2 values in matching colours.

4 Discussion and Conclusions

The MELTNET deep neural network can produce melt rates that closely resemble those calculated by the NEMO ocean model for synthetic geometries that were not part of the training set. When compared to two intermediate complexity melt rate

310 parameterisations, MELTNET outperforms them in terms of both overall NRMSE and correlation, even when parameters in those models are tuned to minimise the misfit for the geometries we test. In terms of area averaged melt rates (Fig 4), MELTNET also performs favorably compared to PICO and PLUME, which both tend to underestimate this value. Since these two models are tuned to minimise the overall NRMSE rather than average melt this is not particularly surprising, but nevertheless highlights the problem with tuning these models based on one metric, leading them to perform poorly in other regards.

315 Correctly predicting spatial patterns of ice shelf melting (as shown by the high correlation of our results to NEMO), rather than just the magnitude, is crucial because the sensitivity of an ice shelf to thinning will vary across that ice shelf (Reese et al., 2018b). Some regions within an ice shelf can be considered entirely 'passive', in that reductions in ice thickness in these areas has no impact on ice flux across the grounding line. On the other hand, perturbations to ice shelf melting within certain highly

buttressed regions, for example in the shear margin of an ice shelf, can have a much greater impact on ice-sheet discharge
320 than other regions such as downstream of an ice stream, despite those being otherwise dynamically important (Feldmann et al., 2021). In general, a small proportion of ice shelves contribute a disproportionately large fraction of the total buttressing force (Reese et al., 2018b).

One important caveat to this work is that MELTNET can only be, at best, as good as the ocean model that it has been trained on. Here, we necessarily treat the ocean model as our ground-truth, since the geometries are entirely synthetic. Training
325 MELTNET on real world observations would be preferable but there are not enough distinct ice shelves, or indeed sufficient observations of melting, for this to be feasible. Thus we consider NEMO melt rates akin to observations and matching these as accurately as possible is our goal. The NEMO ocean model setup has a number of simplifications; for example no representation of sea ice, surface forcing, ocean tides etc. These processes would all impact the melt rate calculation. Some missing processes would be possible to add in with our synthetic geometry approach, but others present more significant challenges.

330 On the other hand, this methodology also provides interesting advantages, since adding complexity to the representation of the ocean model physics can simply be achieved by including more processes in the ocean model. This is in contrast to a typical model where adding new physics is a significant undertaking that can require replacing large sections of code and considerable testing. Furthermore, since the method is not limited in terms of input fields, any missing information required to properly train the network with new physics could easily be added into a new band in the input image. Conversely, processes
335 could be removed by reducing the amount of inputs used to train MELTNET. Doing this would provide insights into which processes are important for producing realistic melt rates, possibly aiding the development of alternative parameterisations.

Further improvements to MELTNET are no doubt possible by altering the network architecture. We developed and tested an architecture that combined both DAE and segmentation components into one network, however this proved harder to optimise than the approach we have presented here. That being said, this possibility could be explored further to simplify the training
340 and application of the MELTNET parameterisation and potentially also increase its accuracy.

The results presented here show a promising first step to a parameterisation for ocean induced melting that shows high fidelity to advanced ocean models with very low computational cost. That being said, more work is required, before applying this to transient ice sheet models. Future work must demonstrate that the network, trained on synthetic geometries, is also capable of reproducing melt rate patterns on real ice shelves based on the limited observations that exist or in comparison to state-of-the-art
345 ocean models. One limiting factor currently is the size of the domain, which at ~502km square is not large enough to cover the very largest ice shelves and include neighbouring open ocean to serve as input for training and prediction. Furthermore, more work is needed to show the equivalence of these synthetic geometries to real ice shelves, include complex bathymetric features such as ice rises or troughs that play an important role in providing access for warm water to the grounding line, and add more processes to the ocean model that is used for training. Subsequently, MELTNET would need extensive testing to ensure
350 that fringe ice shelf configurations never lead to extreme melt rate predictions that are outside of what would be physically plausible. A recent innovation that could help in this regard is the development of neural network emulators constrained, either through the loss function or their architecture to ensure that they do not violate physical laws (e.g. conservation) (Beucler et al., 2021).
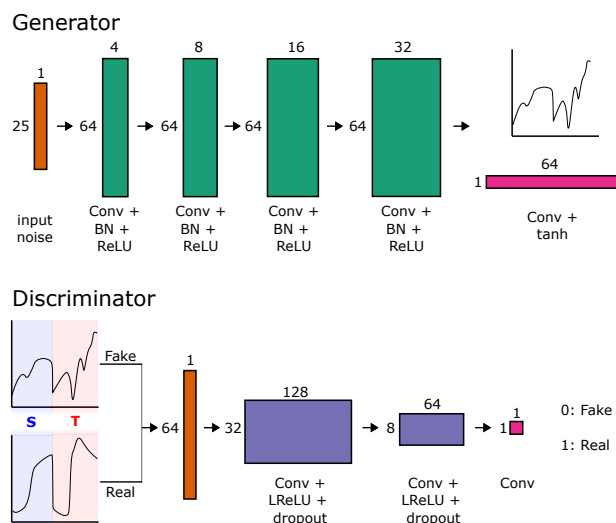
Figure A1. Schematic showing the GAN architecture, used to generate synthetic temperature and salinity profiles from the WOA observations. The Generator network (top) takes a 25x1 random vector and, through a series of convolution layers, outputs a synthetic combined profile. The discriminator network (bottom) is given both real and synthetic profiles and labels these as real or fake. Both networks learn from one another, resulting in a generator network that can create an infinite number of realistic temperature and salinity profiles from random noise.

This work has demonstrated that a deep learning network can be trained to emulate an ocean model in terms of predicted melt rates beneath an Antarctic ice shelf. When applied to a wide range of synthetic geometries, MELTNET agrees closely with the NEMO model that it was trained on, and outperforms other commonly used parameterisations if we assume that the ocean model represents the best estimate of melt rates for a given geometry. These results show that a deep learning emulator may provide useful melt rate estimates for ice sheet models but more work is needed to refine the methodology and test this approach on real ice shelf geometries with observations of melt rates. An accurate and efficient parameterisation of melt rates beneath Antarctic ice shelves is urgently needed to improve the representation of this crucial component of mass loss.

Code availability. All deep learning development and training was done using MATLAB's deep learning toolbox (The MathWorks, 2021). The two intermediate complexity melt-rate parameterisations were implemented in the open-source ice flow model Úa, available at https://doi.org/10.5281/zenodo. The synthetic geometries, generated to train MELTNET, are available from the authors upon request.

Appendix A: Synthetic Temperature and Salinity generation

As described in the methods, rather than using the finite number of observations of temperature and salinity to force our synthetic geometries, we generate synthetic profiles using a GAN. The GAN consists of two networks trained together; a
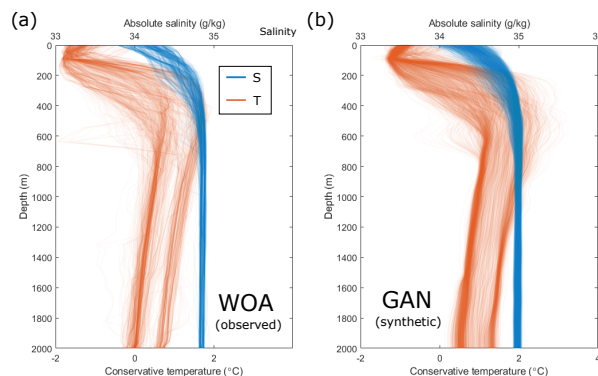
Figure A2. Temperature and salinity profiles (a) extracted from the WOA dataset (Boyer et al.) from the closest 2000m depth cell around Antarctica ($N = 1440$) and (b) generated from the GAN ($N = 5000$), trained on the WOA data shown in (a). WOA data is converted to the TESO10 standard (IOC and IAPSO, 2010), prior to being used to train the GAN.

generator network and a discriminator network. The generator learns to generate synthetic temperature and salinity profiles while the discriminator network attempts to distinguish between real profiles (from the WOA dataset) and the profiles created by the generator. Initially, neither network knows what to do but are in direct competition and learn from each other to improve. At
370 the end of the training process, the generator network has learnt to take a random vector input as a seed and output temperature and salinity profiles that closely resemble the real data. Since the GAN takes a random seed as input, any number of these random seeds can be used to generate the desired number of synthetic profiles.

The specific architecture used, shown in Fig. A1 is a modification of the Deep Convolutional GAN (DCGAN) as proposed by Radford et al. (2016). Temperature and salinity profiles from WOA are concatenated into one vector which the discriminator
375 aims to reproduce and the discriminator learns to differentiate. The discriminator network includes dropout layers with a dropout of 50%, which was necessary to avoid mode collapse. The two networks are trained simultaneously for 500 epochs and reach an equilibrium in which the loss for each stabilises around 0.5. Every available temperature and salinity profile from the WOA dataset, used to train the GAN, is shown in Fig. A2a, together with a sample of synthetic profiles generated by the GAN in Fig. A2b.

380 **Appendix B: Supplementary Figures**
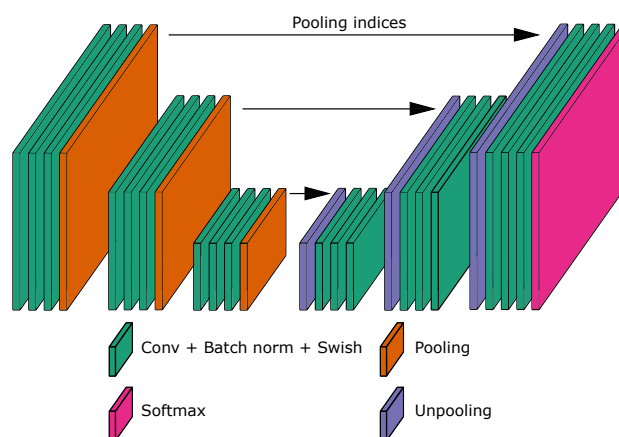
Figure B1. Schematic for the segmentation network used in this study. An input 64x64x4 image goes through layers of convolution, batch normalisation and swish layers in sequences of pooling and unpooling layers. Once trained on NEMO results, the final output is a segmented image consisting of melt rate labels that can then be converted into a melt rate field using the AE network.
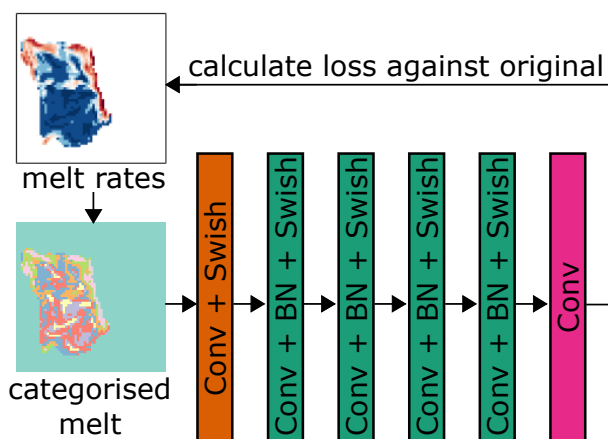
Figure B2. Schematic for the AE net architecture used in this study. A melt rate field, as calculated by NEMO for a given input geometry, is converted to a matrix of discrete melt labels. These labelled melt rates served as the input to the network go through a series of convolution, batch normalisation and swish layers, leading to an output. The loss of this output is calculated against the original melt rate field to train the network to recover a continuous melt rate field from discrete melt rate labels.
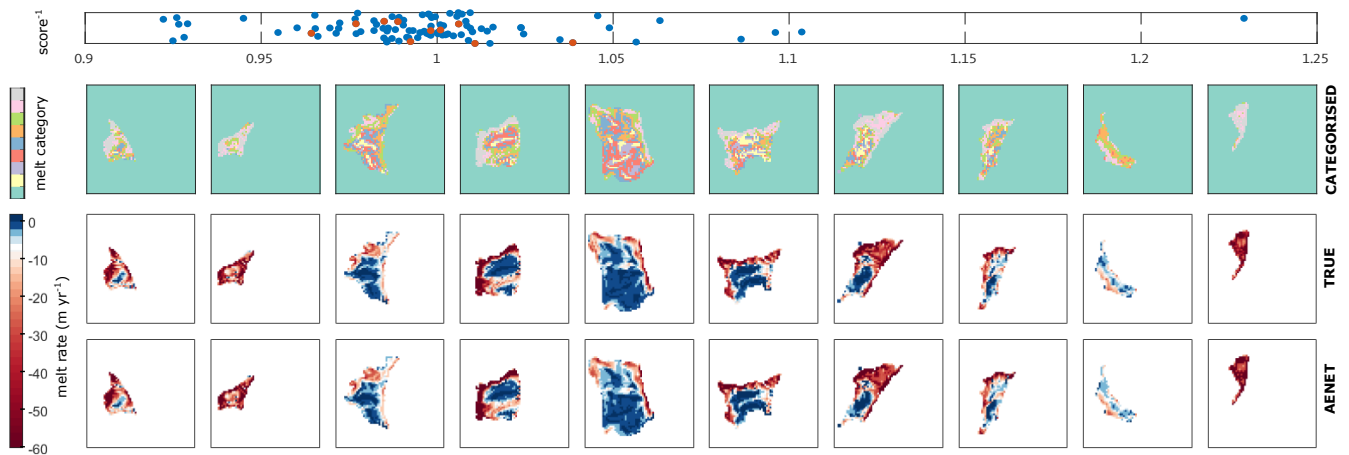
Figure B3. Example of the DAE network used to convert from labelled melt rates (top row) to a continuous melt rate field (true melt rates in the second row, predicted melt rates by the DAE network in the bottom row). Examples shown are selected by evenly sampling the distribution of DAE network scores (all scores shown in the upper scatter plot with sampled scores in red).
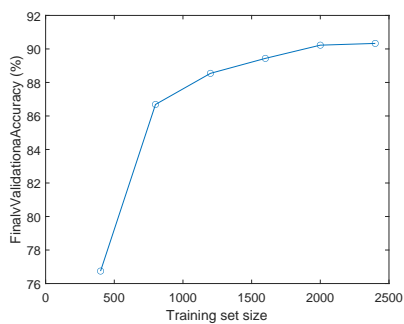
Figure B4. Final validation accuracy of the segmentation net, as a function of the size of the training set (number of unique ice shelf geometry and ocean conditions configurations). Validation accuracy represents the percentage of correctly labelled melt rates.

Table B1. parameters for the two intermediate complexity melt rate models (PICO and PLUME), showing both the originally published values and the optimised values that minimised the NRMSE to NEMO melt rates, as described in the Methods.

Parameter	Model	Value	Original
ρ_i	all	917	
ρ_w	all	1030	
γ_T^*	PICO	0.97e6	2.00e-5 m s^{-1}
C	PICO	1.00e6	0.70e6 m^{6}s^{-1}kg^{-1}
Γ_{TS}	PLUME	2.19e-4	6.00e-4
E_0	PLUME	1.98e-2	3.60e-2

Author contributions. S.R. conceived the study, created the synthetic training sets and developed the deep learning methodology. C. B. setup and ran the ocean modelling component. All authors contributed ideas to analysis of the results and to the writing of the manuscript.

Competing interests. The contact author has declared that neither they nor their co-authors have any competing interests.

Acknowledgements. This work used the ARCHER2 UK National Supercomputing Service (https://www.archer2.ac.uk). S.R. is supported by
385   the PROPHET project, a component of the International Thwaites Glacier Collaboration (ITGC). Support from National Science Foundation
(NSF: Grant 1739031) and Natural Environment Research Council (NERC: Grants NE/S006745/1 and NE/S006796/1). C.B. is supported by
the European Union's Horizon 2020 research and innovation programme under grant agreement no. 820575 (TiPACCs). We are very grateful
to Adrian Jenkins for numerous helpful discussions.

References

390 Asay-Davis, X. S., Cornford, S. L., Durand, G., Galton-Fenzi, B. K., Gladstone, R. M., Gudmundsson, G. H., Hattermann, T., Holland, D. M., Holland, D., Holland, P. R., Martin, D. F., Mathiot, P., Pattyn, F., and Seroussi, H.: Experimental design for three interrelated marine ice sheet and ocean model intercomparison projects: MISMIP v. 3 (MISMIP+), ISOMIP v. 2 (ISOMIP+) and MISOMIP v. 1 (MISOMIP1), Geoscientific Model Development, 9, 2471–2497, https://doi.org/10.5194/gmd-9-2471-2016, 2016.

Badrinarayanan, V., Kendall, A., and Cipolla, R.: SegNet: A Deep Convolutional Encoder-Decoder Architecture for Image Segmentation,
395 IEEE Transactions on Pattern Analysis and Machine Intelligence, 39, 2481–2495, https://doi.org/10.1109/TPAMI.2016.2644615, 2017.

Bernard, B., Madec, G., and Penduff, T. e. a.: Impact of partial steps and momentum advection schemes in a global ocean circulation model at eddy-permitting resolution, Ocean Dynamics, 56, 543–567, https://doi.org/10.1007/s10236-006-0082-1, 2006.

Beucler, T., Pritchard, M., Rasp, S., Ott, J., Baldi, P., and Gentine, P.: Enforcing Analytic Constraints in Neural Networks Emulating Physical Systems, Phys. Rev. Lett., 126, 098 302, https://doi.org/10.1103/PhysRevLett.126.098302, 2021.

400 Boyer, T. P., Garcia, H. E., Locarnini, R. A., Zweng, M. M., Mishonov, A. V., Reagan, J. R., Weathers, K. A., Baranova, O. K., Seidov, D., and Smolyar, I. V.: World Ocean Atlas 2018.

Brenowitz, N. D. and Bretherton, C. S.: Prognostic Validation of a Neural Network Unified Physics Parameterization, Geophysical Research Letters, 45, 6289–6298, https://doi.org/https://doi.org/10.1029/2018GL078510, 2018.

Brenowitz, N. D. and Bretherton, C. S.: Spatially Extended Tests of a Neural Network Parametrization Trained by Coarse-Graining, Journal
405 of Advances in Modeling Earth Systems, 11, 2728–2744, https://doi.org/https://doi.org/10.1029/2019MS001711, 2019.

De Rydt, J., Holland, P. R., Dutrieux, P., and Jenkins, A.: Geometric and oceanographic controls on melting beneath Pine Island Glacier, Journal of Geophysical Research: Oceans, 119, 2420–2438, https://doi.org/https://doi.org/10.1002/2013JC009513, 2014.

Donat-Magnin, M., Jourdain, N. C., Spence, P., Le Sommer, J., Gallée, H., and Durand, G.: Ice-Shelf Melt Response to Changing Winds and Glacier Dynamics in the Amundsen Sea Sector, Antarctica, Journal of Geophysical Research: Oceans, 122, 10 206–10 224,
410 https://doi.org/https://doi.org/10.1002/2017JC013059, 2017.

Dupont, T. K. and Alley, R. B.: Assessment of the importance of ice-shelf buttressing to ice-sheet flow, Geophysical Research Letters, 32, https://doi.org/https://doi.org/10.1029/2004GL022024, 2005.

Edwards, T., Nowicki, S., and Marzeion, B. e. a.: rojected land ice contributions to twenty-first-century sea level rise, Nature, 593, 74–82, https://doi.org/10.1038/s41586-021-03302-y, 2021.

415 Favier, L., Jourdain, N. C., Jenkins, A., Merino, N., Durand, G., Gagliardini, O., Gillet-Chaulet, F., and Mathiot, P.: Assessment of sub-shelf melting parameterisations using the ocean–ice-sheet coupled model NEMO(v3.6)–Elmer/Ice(v8.3), Geoscientific Model Development, 12, 2255–2283, https://doi.org/10.5194/gmd-12-2255-2019, 2019.

Feldmann, J., Reese, R., Winkelmann, R., and Levermann, A.: Shear-margin melting causes stronger transient ice discharge than ice-stream melting according to idealized simulations, The Cryosphere Discussions, 2021, 1–28, https://doi.org/10.5194/tc-2021-327, 2021.

420 Garbe, J., Albrecht, T., Levermann, A., Donges, J., and Winkelmann, R.: The hysteresis of the Antarctic Ice Sheet, Nature, 585, 538–544, https://doi.org/10.1038/s41586-020-2727-5, 2020.

Goldberg, D. N., Gourmelen, N., Kimura, S., Millan, R., and Snow, K.: How Accurately Should We Model Ice Shelf Melt Rates?, Geophysical Research Letters, 46, 189–199, https://doi.org/https://doi.org/10.1029/2018GL080383, 2019.

Goodfellow, I., Pouget-Abadie, J., Mirza, M., Xu, B., Warde-Farley, D., Ozair, S., Courville, A., and Bengio, Y.: Generative Adversarial Nets,
425 in: Advances in Neural Information Processing Systems, edited by Ghahramani, Z., Welling, M., Cortes, C., Lawrence, N., and Weinberger,

K. Q., vol. 27, Curran Associates, Inc., https://proceedings.neurips.cc/paper/2014/file/5ca3e9b122f61f8f06494c97b1afccf3-Paper.pdf, 2014.

Gudmundsson, G. H., Krug, J., Durand, G., Favier, L., and Gagliardini, O.: The stability of grounding lines on retrograde slopes, The Cryosphere, 6, 1497–1505, https://doi.org/10.5194/tc-6-1497-2012, 2012.

Holland, P. R., Jenkins, A., and Holland, D. M.: The Response of Ice Shelf Basal Melting to Variations in Ocean Temperature, Journal of Climate, 21, 2558 – 2572, https://doi.org/10.1175/2007JCLI1909.1, 2008.

IOC, S. and IAPSO: The international thermodynamic equation of seawater – 2010: Calculation and use of thermodynamic properties, Intergovernmental Oceanographic Commission, Manuals and Guides, 56, 196, 2010.

IPCC: IPCC, 2021: Climate Change 2021: The Physical Science Basis, Cambridge University press, 2021.

Jenkins, A.: A one-dimensional model of ice shelf-ocean interaction, Journal of Geophysical Research: Oceans, 96, 20 671–20 677, https://doi.org/https://doi.org/10.1029/91JC01842, 1991.

Jenkins, A., S. D. D. P. e. a.: West Antarctic Ice Sheet retreat in the Amundsen Sea driven by decadal oceanic variability, Nature Geosci., 11, 733–738, https://doi.org/10.1038/s41561-018-0207-4, 2018.

Jordan, J. R., Holland, P. R., Goldberg, D., Snow, K., Arthern, R., Campin, J.-M., Heimbach, P., and Jenkins, A.: Ocean-Forced Ice-Shelf Thinning in a Synchronously Coupled Ice-Ocean Model, Journal of Geophysical Research: Oceans, 123, 864–882, https://doi.org/https://doi.org/10.1002/2017JC013251, 2018.

Jourdain, N. C., Asay-Davis, X., Hattermann, T., Straneo, F., Seroussi, H., Little, C. M., and Nowicki, S.: A protocol for calculating basal melt rates in the ISMIP6 Antarctic ice sheet projections, The Cryosphere, 14, 3111–3134, https://doi.org/10.5194/tc-14-3111-2020, 2020.

Khairoutdinov, M. F. and Randall, D. A.: Cloud Resolving Modeling of the ARM Summer 1997 IOP: Model Formulation, Results, Uncertainties, and Sensitivities, Journal of the Atmospheric Sciences, 60, 607 – 625, https://doi.org/10.1175/1520-0469(2003)060<0607:CRMOTA>2.0.CO;2, 2003.

Kreuzer, M., Reese, R., Huiskamp, W. N., Petri, S., Albrecht, T., Feulner, G., and Winkelmann, R.: Coupling framework (1.0) for the PISM (1.1.4) ice sheet model and the MOM5 (5.1.0) ocean model via the PICO ice shelf cavity model in an Antarctic domain, Geoscientific Model Development, 14, 3697–3714, https://doi.org/10.5194/gmd-14-3697-2021, 2021.

Lazeroms, W. M. J., Jenkins, A., Gudmundsson, G. H., and van de Wal, R. S. W.: Modelling present-day basal melt rates for Antarctic ice shelves using a parametrization of buoyant meltwater plumes, The Cryosphere, 12, 49–70, https://doi.org/10.5194/tc-12-49-2018, 2018.

Madec, G. and Team, N. S.: NEMO ocean engine, Institut Pierre-Simon Laplace (IPSL), https://doi.org/10.5281/zenodo.1464816.

Mathiot, P., Jenkins, A., Harris, C., and Madec, G.: Explicit representation and parametrised impacts of under ice shelf seas in the z^* coordinate ocean model NEMO 3.6, Geoscientific Model Development, 10, 2849–2874, https://doi.org/10.5194/gmd-10-2849-2017, 2017.

Naughten, K. A., De Rydt, J., Rosier, S. H. R., Jenkins, A., Holland, P. R., and Ridley, J. K.: Two-timescale response of a large Antarctic ice shelf to climate change, Nature Communications, 12, 2041–1723, https://doi.org/https://doi.org/10.1038/s41467-021-22259-0, 2021.

Nilsson, J., Jakobsson, M., Borstad, C., Kirchner, N., Björk, G., Pierrehumbert, R. T., and Stranne, C.: Ice-shelf damming in the glacial Arctic Ocean: dynamical regimes of a basin-covering kilometre-thick ice shelf, The Cryosphere, 11, 1745–1765, https://doi.org/10.5194/tc-11-1745-2017, 2017.

O'Gorman, P. A. and Dwyer, J. G.: Using Machine Learning to Parameterize Moist Convection: Potential for Modeling of Climate, Climate Change, and Extreme Events, Journal of Advances in Modeling Earth Systems, 10, 2548–2563, https://doi.org/https://doi.org/10.1029/2018MS001351, 2018.

Pritchard, H. D., Ligtenberg, S. R. M., Fricker, H. A., Vaughan, D. G., van den Broeke, M. R., and Padman, L.: Antarctic ice-sheet loss driven
465   by basal melting of ice shelves, Nature, 484, 502–505, https://doi.org/10.1038/nature10968, 2012.

Radford, A., Metz, L., and Chintala, S.: Unsupervised Representation Learning with Deep Convolutional Generative Adversarial Networks,
2016.

Ramachandran, P., Zoph, B., and Le, Q. V.: Searching for Activation Functions, CoRR, abs/1710.05941, http://arxiv.org/abs/1710.05941,
2017.

470 Rasp, S., Pritchard, M. S., and Gentine, P.: Deep learning to represent subgrid processes in climate models, Proceedings of the National
Academy of Sciences, 115, 9684–9689, https://doi.org/10.1073/pnas.1810286115, 2018.

Reese, R., Albrecht, T., Mengel, M., Asay-Davis, X., and Winkelmann, R.: Antarctic sub-shelf melt rates via PICO, The Cryosphere, 12,
1969–1985, https://doi.org/10.5194/tc-12-1969-2018, 2018a.

Reese, R., Gudmundsson, G. H., Levermann, A., and Winkelmann, R.: The far reach of ice-shelf thinning in Antarctica, Nature Climate
475   Change, 8, 53–57, https://doi.org/10.1038/s41558-017-0020-x, 2018b.

Seroussi, H., Nakayama, Y., Larour, E., Menemenlis, D., Morlighem, M., Rignot, E., and Khazendar, A.: Continued retreat of
Thwaites Glacier, West Antarctica, controlled by bed topography and ocean circulation, Geophysical Research Letters, 44, 6191–6199,
https://doi.org/https://doi.org/10.1002/2017GL072910, 2017.

Shepherd, A., Ivins, E., Rignot, E., Smith, B., and van den Broeke, M. e. a.: Mass balance of the Antarctic Ice Sheet from 1992 to 2017,
480   Nature, 558, 219–222, https://doi.org/10.1038/s41586-018-0179-y, 2018.

Smith, R. S., Mathiot, P., Siahaan, A., Lee, V., Cornford, S. L., Gregory, J. M., Payne, A. J., Jenkins, A., Holland, P. R., Ridley, J. K.,
and Jones, C. G.: Coupling the U.K. Earth System Model to Dynamic Models of the Greenland and Antarctic Ice Sheets, Journal of
Advances in Modeling Earth Systems, 13, e2021MS002 520, https://doi.org/https://doi.org/10.1029/2021MS002520, e2021MS002520
2021MS002520, 2021.

485 Stevens, B. and Bony, S.: What Are Climate Models Missing?, Science, 340, 1053–1054, https://doi.org/10.1126/science.1237554, 2013.

The MathWorks, I.: Deep Learning Toolbox, Natick, Massachusetts, United State, https://www.mathworks.com/help/deeplearning/, 2021.

Thoma, M., Determann, J., Grosfeld, K., Goeller, S., and Hellmer, H. H.: Future sea-level rise due to projected ocean warm-
ing beneath the Filchner Ronne Ice Shelf: A coupled model study, Earth and Planetary Science Letters, 431, 217–224,
https://doi.org/https://doi.org/10.1016/j.epsl.2015.09.013, 2015.

490 Thomas, R. H.: Ice Shelves: A Review, Journal of Glaciology, 24, 273–286, https://doi.org/10.3189/S0022143000014799, 1979.

Zhang, K., Zuo, W., Chen, Y., Meng, D., and Zhang, L.: Beyond a Gaussian Denoiser: Residual Learning of Deep CNN for Image Denoising,
IEEE Transactions on Image Processing, 26, 3142–3155, https://doi.org/10.1109/tip.2017.2662206, 2017.